Self-Powered Direct Muscle Stimulation Using a Triboelectric Nanogenerator (TENG) Integrated with a Flexible Multiple-Channel Intramuscular Electrode

Jiahui Wang,[†,‡,§,⊥,¶] Hao Wang,[†,‡,§,⊥,¶] Nitish V. Thakor,[†,‡] and Chengkuo Lee*[,†,‡,§,⊥]

[†]Department of Electrical and Computer Engineering, National University of Singapore, 4 Engineering Drive 3, Singapore 117583, Singapore

[‡]Singapore Institute for Neurotechnology, National University of Singapore, 28 Medical Drive, #05-COR, Singapore 117456, Singapore

[§]Hybrid-Integrated Flexible (Stretchable) Electronic Systems Program, National University of Singapore, 5 Engineering Drive 1, Singapore 117608, Singapore

[⊥]NUS Suzhou Research Institute (NUSRI), Suzhou Industrial Park, Suzhou 215123, P. R. China

ⓢ *Supporting Information*

ABSTRACT: Muscle function loss can result from multiple nervous system diseases including spinal cord injury (SCI), stroke, and multiple sclerosis (MS). Electrical muscle stimulation is clinically employed for rehabilitative and therapeutic purpose and typically requires mA-level stimulation current. Here, we report electrical muscle stimulation, which is directly powered by a stacked-layer triboelectric nanogenerator (TENG) through a flexible multiple-channel intramuscular electrode. This multiple-channel intramuscular electrode allows mapping of motoneurons that is sparsely distributed in the muscle tissue and thus enables high efficiency TENG muscle stimulation, although the short-circuit current of the TENG is only 35 μA. With a stimulation efficiency matrix, we find the electrical muscle stimulation efficiency is affected by two factors, namely, the electrode-motoneuron position, and the stimulation waveform polarity. To test whether it is a universal phenomenon for electrical stimulation, we then further investigate with the conventional square wave current stimulation and confirm that the stimulation efficiency is also affected by these two factors. Thus, we develop a self-powered direct muscle stimulation system with a TENG as power source and waveform generator, and a multiple-channel intramuscular electrode to allow motoneuron mapping for stimulation efficiency optimization. We believe such self-powered system could be potentially used for rehabilitative and therapeutic purpose to treat muscle function loss.

KEYWORDS: *electrical muscle stimulation, triboelectric direct stimulation without rectification, self-powered, stimulation efficiency, electrode-motoneuron position, stimulation waveform*
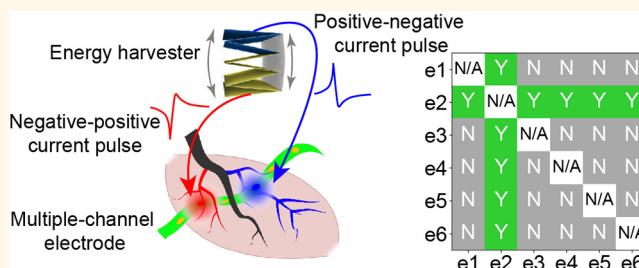
Recent progress in wearable medical devices that employ flexible materials has enabled long-term fitness monitoring and medical diagnostics by providing continuous measurement of human vital signs. Various skin-patch sensors are developed to monitor body motion,[1−4] sweat electrolytes and metabolites,[5−7] blood pressure,[8,9] and surface electrophysiology signals.[10,11] Further integration with wireless transmission[12] and energy harvesting[13−17] technology makes long-term stand-alone wearable medical systems possible. In addition, implantable devices made of biocompatible flexible materials directly contact with biological tissues and organs to perform delicate sensing and deliver therapeutic interventions.

For instance, the emerging soft deformable actuators wrap around the organs to assist normal functions by mechanically squeezing the failing heart[18] or bladder.[19] The more common therapeutic implantable medical devices deliver electrical stimulation to induce action potentials (APs) in biological tissues, including soft penetrating carbon nanofiber (CNF) electrode[20] and graphene oxide (GO) electrode[21] for deep

brain stimulation (DBS), and flexible polyimide electrode[22] for peripheral nerve stimulation. The intrinsic biocompatible and flexible properties of these implantable medical devices match well with the biological tissues, making them good candidates to minimize tissue damage and thus achieve long-term therapeutic interventions. Various flexible electrodes were developed including transverse intrafascicular multichannel electrode (TIME),[23] cuff electrode,[24] ribbon electrode[25] to interface with peripheral nerves, and ultraflexible high density electrode arrays to interface with the cortex.[26,27] The emerging of neural electrodes has contributed to the recent development of novel therapeutic interventions to develop brain−machine interface[28] and treat spinal cord injury.[29,30] Yet, one area of huge unmet clinical need is to develop rehabilitative and therapeutic implantable medical systems for patients with muscle function loss.

Muscle function loss is characterized as symptoms of abnormal muscle movement, and the complete loss of muscle function is termed paralysis. Nervous system diseases, including spinal cord injury (SCI), stroke, and multiple sclerosis (MS), can lead to a loss of control over otherwise intact neuromuscular systems and cause muscle function loss,[31] which dramatically deteriorates a patient's life quality. Depending on the intervention protocols, electrical muscle stimulation is a currently available method for either rehabilitative or therapeutic purpose. There are two treatment scenarios for muscle function loss. First, when muscles lose neural drive, they atrophy rapidly, and electrical muscle stimulation has been used in attempts to prevent or reverse the atrophy.[32] Second, on top of the initial rehabilitative interventions, functional electrical stimulation (FES) on muscle aims to further recover meaningful movements to achieve complicated tasks of grasping and walking.[33] As compared to electrical nerve stimulation, direct electrical muscle stimulation selectively delivers therapeutic interventions to the affected muscles. The conventional muscle stimulation electrodes include epimysial electrode[34−36] and single channel intramuscular electrode,[37−39] which lacks the capability to access different muscle fibers.

To build an implantable electrical muscle stimulation system, a reliable power source is of crucial importance. Some feasible power supply solutions have been investigated, including the implantable batteries that suffer from a limited lifespan and require surgical procedure for replacement,[40] and external power sources, which wirelessly provide energy to the implants via ultrasound[41,42] or electromagnetic[43] coupling method. Alternatively, harnessing the rich body energy to power the implants makes self-sustainable power supply possible and opens possibilities to explore various energy-harvesting mechanisms. For example, mechanical energy harvesting from organ motions by piezoelectric device,[44−49] and chemical energy harvesting with catalyzed glucose fuel cells[50−52] have been reported. Among the mechanical energy harvesting devices, triboelectric nanogenerators (TENGs) are widely explored as implantable power source. In TENGs, energy conversion is achieved by coupling between the triboelectric effect and the electrostatic effect, and thus, the TENGs act as charge pumps, in which current flows back and forth between the two electrodes in alternating current (AC) characteristics.[53−58] The *in vivo* demonstrations of implantable TENGs made of biocompatible materials harvesting mechanical energy from heartbeat and respiratory motion have validated the possibilities of integrating TENGs as power

source in implantable medical system.[59−64] Energy harvested from body energy can directly stimulate biological tissues without any rectification. On the cell level, Guo et al. showed enhanced neural differentiation powered by TENG.[65] In addition, Hwang et al. first demonstrated deep brain stimulation with piezoelectric energy harvester, and Fu et al. and Dai et al. demonstrated rat sensory cortex stimulation with TENGs.[66,67] For peripheral nerve stimulation, Zhang et al. first demonstrated the electrical activation of the frog sciatic nerve directly powered by a TENG.[68] Then Lee et al. further investigated the high electrical activation efficiency as well as the selectivity of the rat sciatic nerve powered by TENGs.[69,70]

Despite the above pioneering work demonstrating direct peripheral nerve and cortex stimulation with TENGs, it still remains unknown whether TENGs can directly activate muscles. Different from the peripheral nerves and cortex, which are mainly constituted of excitable neurons and easy to be electrically activated, muscles have 50 to 500 motor units, each of which consists of one motoneuron plus a few hundred muscle fibers that it innervates.[33] Since the threshold charge for directly eliciting muscle fiber action potentials is much greater than the threshold for producing action potentials in motoneurons, electrical muscle stimulation operates under the fundamental principle that motoneurons are activated to subsequently drive the muscle fibers.[71] As a result, electrical muscle stimulation typically requires mA-level stimulation current.[71] Considering such sparse spatial distribution of excitable motoneurons in muscle tissue, it will require high stimulation efficiency to achieve electrical stimulation with μA-level current output from TENGs, which represents a huge challenge for conventional stimulation electrode design of epimysial electrode and single channel intramuscular electrode. For epimysial electrode, electric field goes through lossy muscle tissues before reaching the distributed motoneurons, and thus high current is required. Similarly, single channel intramuscular electrode also faces difficulty in finding the optimum position to effectively stimulate the distributed motoneurons. Thus, achievement of μA-level direct muscle stimulation using TENGs necessitates a muscle electrode design, which can access the sparsely distributed motoneurons to optimize stimulation efficiency.

Here, we propose a flexible multiple-channel intramuscular electrode design, which enables spatial mapping of motoneuron distribution in the muscle tissue. With this intramuscular electrode, we demonstrate direct electrical muscle stimulation using a stacked-layer TENG and find the TENG stimulation efficiency is affected by two factors, namely, the electrode-motoneuron position, and stimulation waveform polarity. Then we further investigate how these two factors affect the stimulation efficiency, with conventional square wave stimulation.

RESULTS AND DISCUSSION

System, Device Configuration, and Working Mechanism. Figure 1 shows the concept of electrical muscle stimulation, which is directly powered by TENGs without further rectification. A stacked-layer TENG structure is chosen, as this structure deforms with applied pressure to turn mechanical energy into electrical energy. Such mechanical deformation can be easily incorporated into human body motions. For example, the TENGs can be pressed by feet during walking or tapped by hands which offers more control flexibility so as the user can voluntarily control the timing of
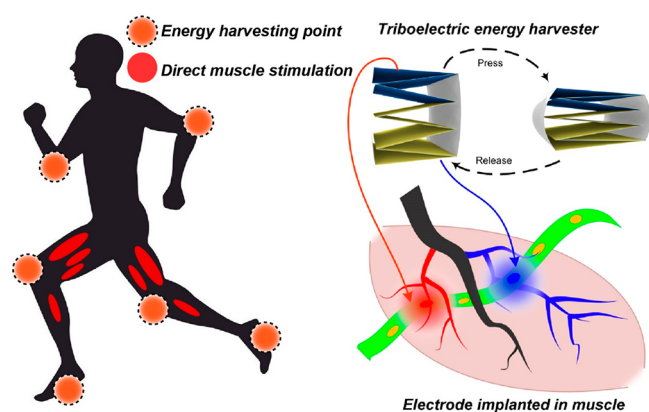
Figure 1. Schematic diagram that shows the concept of electrical muscle stimulation directly powered by a TENG.

TENGs activation. By connecting the TENGs output to multiple intramuscular electrodes, users can harvest mechanical energy from body motions to electrically stimulate muscles for either rehabilitation or therapeutic purpose.

The detailed fabrication process of TENGs can be found in Figure S1. For mechanical support during back and forth pressing operation, a PET sheet is folded in zigzag structure to store the mechanical deformation energy in the form of elastic energy so that the TENGs can automatically revert to the original position after each pressing. Then aluminum films are attached to each surface of the folded PET sheet to serve as electrodes for charge output. In a pair of the aluminum films, the first aluminum film simultaneously serves dual function of both electrode and active triboelectric surface, while an additional PTFE film is assembled on top of the second aluminum film to serve as triboelectric surface. To confine the structure, a PET film is applied to encompass the stacked-layer TENG. The stacked-layer TENG comes in a 10 cm by 10 cm square shape, and 11 contacting sides are achieved by using the zigzag PET sheet.

The flexible multiple-channel intramuscular electrode is fabricated with microelectromechanical systems (MEMS) technology using photoresistive polyimide as substrate. It consists of polyimide-gold-polyimide in two long ribbon structure connected in the middle. Before implantation, the two long ribbon structures are folded from the middle to form a loop, and a suture wire is threaded in the loop to assist implantation of the electrode into the muscle. During *in vivo* implantation, the suture wire is threaded in the muscle tissue to pull the electrode into the muscle. The detailed fabrication process of the intramuscular electrode is shown in Figure S2. The electrode sites are 300 μm in diameter, and the distance between two adjacent electrode sites is 1 mm.

In electrical stimulation, current source is generally preferred rather than voltage source, as the contact impedance between the stimulation electrodes and biological tissues may vary. To enhance the current output of the TENG device, triboelectric energy harvesters are connected in parallel structure. In the pressing phase, layers of triboelectric energy harvesters contact with each other to generate triboelectric surface charge on PTFE and the aluminum film, and the resultant current flows through the electrode to stimulate muscle tissue. In the releasing phase, accumulated triboelectric surface charge flows in the reverse direction, and the resultant current output has the opposite polarity as compared to the pressing phase. Thus,

during one cycle of pressing and releasing, TENG sequentially generates current peaks of the opposite polarities. Depending on the electrode connection, an electrode will experience either positive−negative or negative−positive current stimulation. Since the polarity of stimulation current waveform dramatically affects depolarization of the neuron membrane, we will study the stimulation efficiency difference under positive−negative and negative−positive current waveform in the later sections.

Benchtop Characterization of TENGs and Intramuscular Electrode. The current output capability of the TENGs (Figure 2a) is important for the success of electrical muscle stimulation. To characterize the output capability of the TENGs, we measured open-circuit voltage output using an oscilloscope (DSOX3034 A, Agilent Technologies), and short-circuit current output with a low noise current preamplifier (SR570, Stanford Research Systems). Figure 2b shows the open-circuit voltage output of 47 V when the TENG was tapped. Figure 2c shows the short-circuit current output of 35 μA. Then load resistance of different value was connected in series with the TENG, and voltage was measured across the load resistance. By calculating the power dissipation in the load resistance, power output of the TENG was characterized. The peak power output of the TENG was 95 μW at the load resistance of 2.8 MΩ.

Here, it remains a question whether the measured short-circuit current output of 35 μA well characterizes the current deliver capability of the TENGs when connected to electrodes for muscle stimulation. From the power output curve (Figure 2d), we can have a rough idea of the inner impedance of the TENG, which should match with the load resistance of 2.8 MΩ that generates the peak power output. During *in vivo* stimulation, the electrode-tissue impedance typically falls in the range of several kΩ, which is much lower than the inner impedance of the TENG and can be approximated as short circuit. Thus, the short-circuit current output of 35 μA well characterizes the current flowing into the muscle tissue when directly powered by the TENGs.

Since the flexible multiple-channel intramuscular electrode (Figure 2e) is designed to be implanted in skeletal muscle tissue, which flexes and contracts, the electrochemical and mechanical properties of the polyimide substrate and metal interconnects are important to ensure stable *in vivo* testing. Electrochemical impedance spectroscopy (EIS) was conducted using potentiostat (ZAHNER-elektrik, Electrochemical Workstation ZENNIUM E, German). Figure 2f shows the impedance of 300 μm-diameter electrode sites. At 1 kHz, which is a fundamental frequency of biological relevance in action potentials, the impedance magnitude was below 10 kΩ, which was suitable for current delivery in the muscle tissue. Mechanical testing of polyimide failure strain and sustainable metal interconnect under stretching and bending test were performed using computer-controlled tensile and compression test system (Mecmesin, MultiTest 2.5-i, UK). Figure 2g shows the polyimide and metal interconnect failure strain. The electrode was fixed on the computer-controlled tensile and compression test system with original length, and then one side of the electrode was pulled up to induce stretching. During the stretch test, a multimeter was connected to the electrode site to measure the impedance. Once the impedance abruptly increased, we would know the mechanical failure of the metal interconnect happened. Figure 2h demonstrates the stability of electrode impedance during repeated bending test. Similar to the mechanical measurement in Figure 2g, the
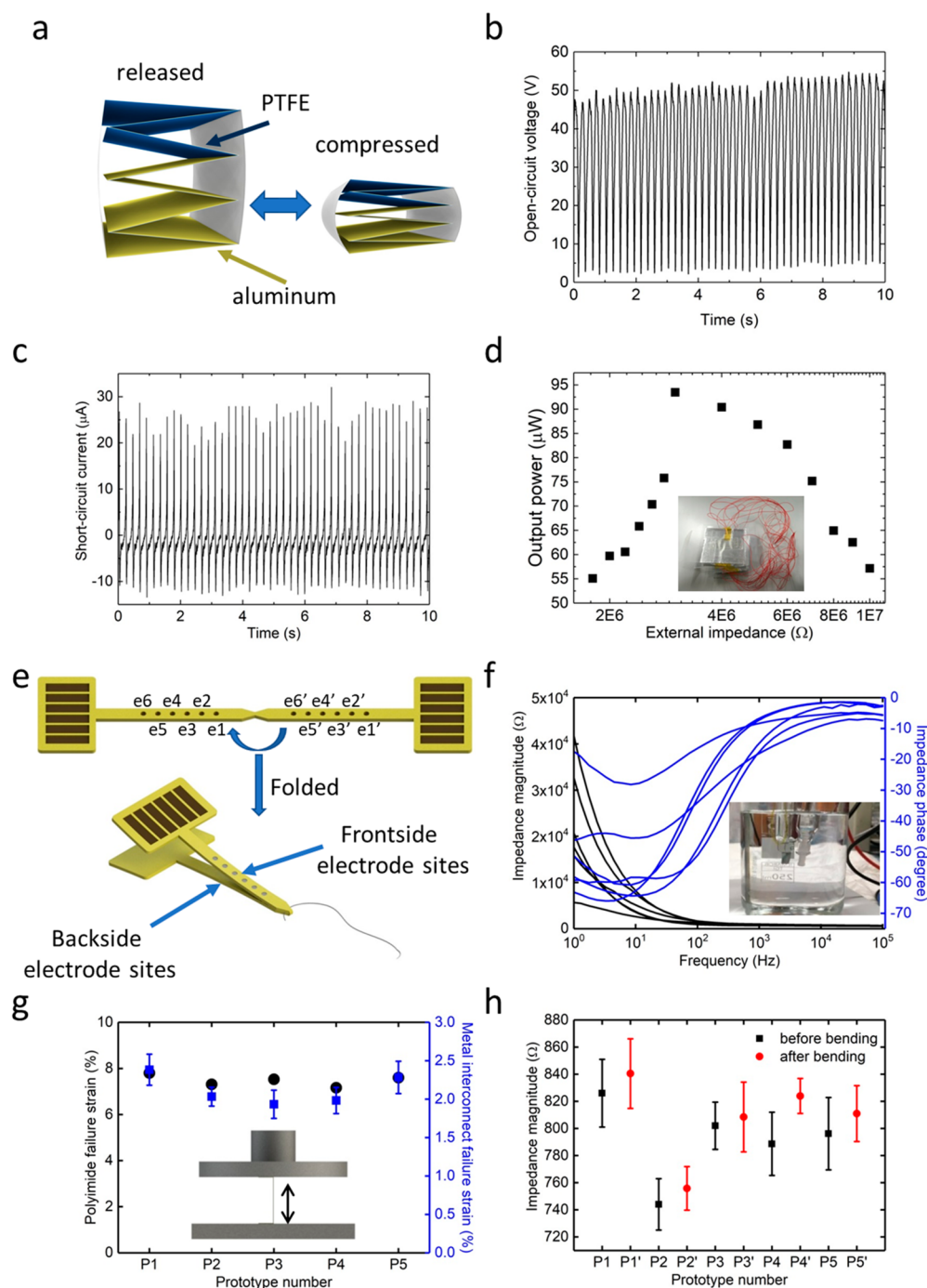
Figure 2. Benchtop characterization of TENG and electrode. (a) Illustration of TENG. (b) Open-circuit voltage. (c) Short-circuit current. (d) Power output with load resistance of the TENG. (e) Illustration of the electrode. (f) Electrochemical impedance spectroscopy. (g) Mechanical testing of polyimide and metal interconnect failure strain. (h) Bending test of the electrode.

electrode was fixed on the computer-controlled tensile and compression test system with original length at first. However, instead of exerting pulling deformation on the electrode, bending was exerted to induce 50% length bending each time. The bending was repeated for 100 times. Impedance of the electrode was monitored before and after the bending test. The impedance remained stable after the repeated bending test. Thus, in the practical applications, although stretching needs to be avoided, bending was acceptable for the electrode.

***In Vivo* Mapping of TENG Stimulation Capability and Efficiency.** We performed *in vivo* experiment to test whether

the 35 μA TENG short-circuit current output was enough to electrically activate muscle through the flexible intramuscular electrode. Figure 3a shows the *in vivo* testing setup. Since the rat tibias anterior (TA) muscle is easy to access and the excitation of the TA muscle induces leg forward kicking movement, we chose it to demonstrate TENG electrical muscle stimulation. The flexible intramuscular electrode was sutured in the TA muscle belly with the help of a suture wire, and a knot was made to fix the electrode (Figure 3b). On the long strip of the flexible intramuscular electrode, only the electrode sites were exposed to contact muscle tissue, and the
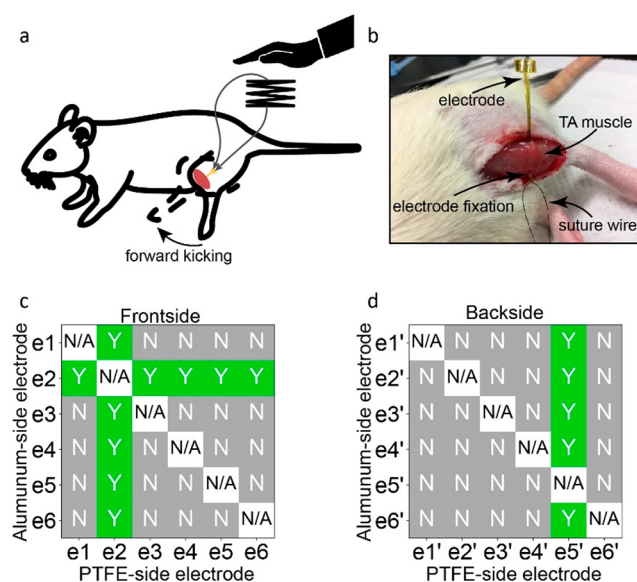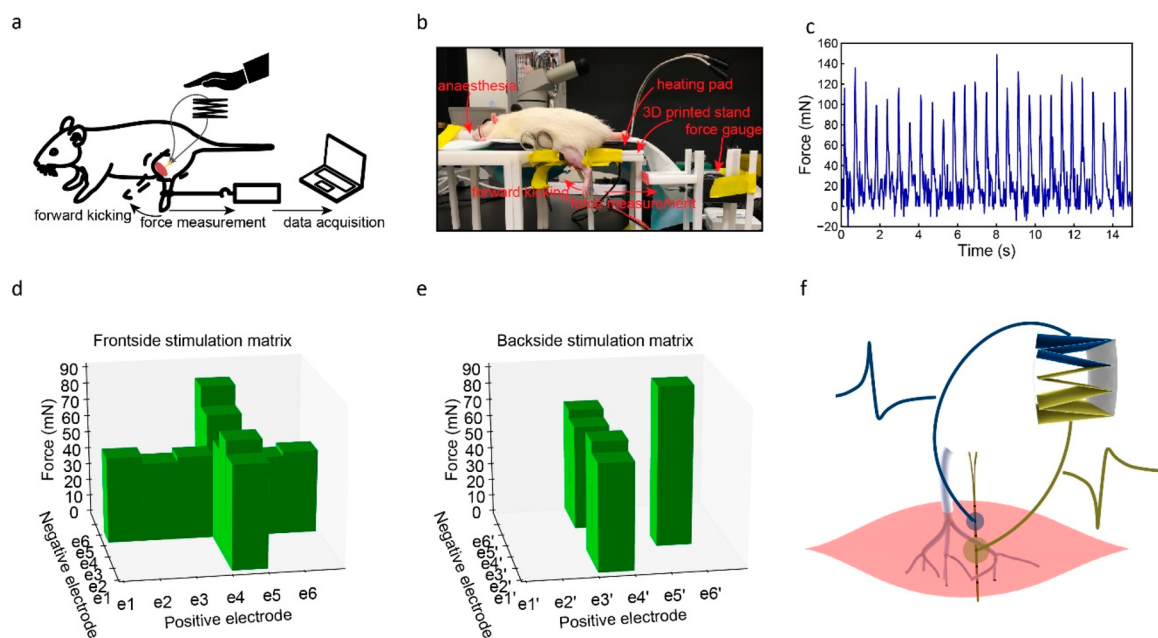
Figure 3. *In vivo* mapping of TENG stimulation capability. (a) Schematic of testing setup, the TENG output directly powers two electrode sites. (b) Electrode implantation. (c) Stimulation capability matrix using the frontside electrode. (d) Stimulation capability matrix using the backside electrode.

interconnect between the electrode site and connection pad was incapsulated. With an FPC connector (Figure S3), the TENG was connected to deliver current stimulation through any two electrode sites. By hand tapping on the TENG, the TENG current output was generated. This TENG current output was directly connected to the flexible intramuscular electrode without further rectification.

Electrical muscle stimulation employed bipolar structure, which requires two stimulation electrode sites to form a close loop. The flexible intramuscular electrode has two sides, and

each side has six electrode sites facing outward to the muscle tissue. Supposedly, any two channels from the total 12 electrode sites could be chosen to deliver current stimulation. However, considering the electrode sites on two sides were separated by insulating polyimide substrate and current could not flow through the polyimide substrate, only electrode sites on the same side were chosen to form the bipolar stimulation structure. Thus, on each side, there were 15 ways to pick two channels out of six electrode sites. We further define the channel connected to the TENG PTFE terminal as PTFE-side electrode, and the channel connected to the TENG aluminum terminal as aluminum-side electrode. By flipping the electrode connection, we have 30 ways of bipolar structure to connect two channels out of six electrodes sites on one side of the flexible electrode to the TENG. Considering the two-side design of the flexible electrode, we had in total 60 ways of bipolar connection. This enabled us to try different electrode site combinations to get access to motoneurons sparsely distributed in the muscle tissue.

To have a clear view on whether TENG could excite TA muscle when different bipolar structure was used, we summarized the stimulation result in a stimulation capability matrix. In the stimulation capability matrix, the PTFE-side electrode is on the *x*-axis and negative electrode is on the *y*-axis. If the TENG induces muscle contraction with a certain bipolar structure (Movie S1), this bipolar structure is marked as 'Y' in green (Figure 3c,d). One interesting phenomenon is that TENG could activate muscle contraction when a specific electrode site was used. In frontside stimulation, only when e2 was used, TENG could induce muscle contraction. While in backside stimulation, only when e5′ was used, TENG could electrically activate muscle. Such observations indicated the electrode-motoneuron position, and e2 and e5′ were closer to motoneurons to induce effective electrical stimulation with the relatively low current output of 35 μA from the TENG. While for other electrode sites that were far away from the

Figure 4. *In vivo* mapping of TENG stimulation efficiency. (a) Schematic of testing setup with force measurement. (b) *In vivo* testing setup. (c) Force profile measured when TENG directly powers muscle stimulation. (d) Stimulation efficiency matrix using the frontside electrode. (e) Stimulation efficiency matrix using the backside electrode. (f) Schematic of unsymmetrical stimulation at the two stimulation electrodes.
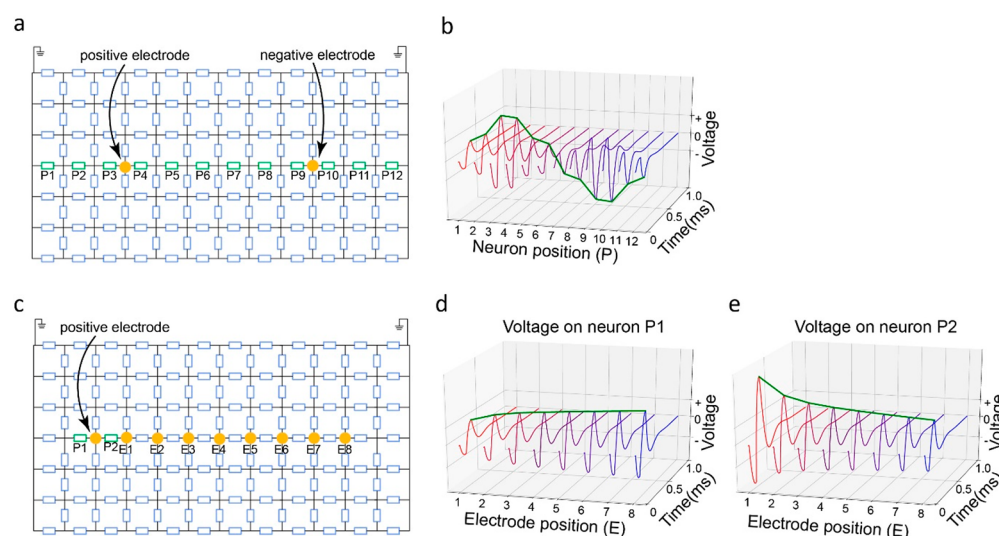
Figure 5. Modeling of voltage waveform in response to different electrode-motoneuron position. (a) Modeling circuit. Voltage on motoneurons at position P1−P12 is studied. (b) Voltage waveforms measured from motoneurons at position P1−P12. (c) Modeling circuit. Electrode distance is increased from E1 to E8. (d) Voltage waveforms measured from motoneuron P1 which is outside the stimulation electrodes. (e) Voltage waveforms measured from motoneuron P1, which is in between the stimulation electrodes.

motoneurons, the low current stimulation from the TENG had to pass through lossy muscle tissue and failed to reach the motoneurons.

This measurement validated the possibility of electrical muscle stimulation with direct powering from the TENG. Furthermore, the observations that specific electrode site had to be involved to induce successful electrical stimulation necessitates the design of this flexible multiple-channel intramuscular electrode, as the mapping of electrode-motoneuron position is of crucial importance to the electrical muscle stimulation with TENG. Another interesting observation is that in the stimulation capability matrix in Figure 3c is symmetrical, while the matrix in Figure 3d is asymmetrical. It indicates the connection of electrodes affects the stimulation capability of the TENG. However, with the simple 0/1 information in Figure 3c, we cannot tell whether flipping the electrode connection affects the generated force output. To solve this issue, we further integrated force measurement (Figure 4a,b) to expand the stimulation capability matrix to a stimulation efficiency matrix, to allow more quantified study.

We expand the 2D stimulation capability matrix to a 3D stimulation efficiency matrix, with the additional z-axis of generated force amplitude information. An example of measured force profile is shown in Figure 4c (Movie S2). For frontside stimulation in Figure 4d, all the successful TENG muscle stimulation involved e4. However, the stimulation efficiency matrix is asymmetrical, meaning that when flipping the electrode connection, the generated force output differed. In Figure 4e, the stimulation efficiency matrix is more asymmetrical. When e3′ was used as the PTFE-side electrode, TENG could induce muscle contraction with e1′, e2′, e4′, and e5′ as aluminum-side electrode. However, when e3′ was used the aluminum-side electrode, TENG could only activate muscle with e5′ as PTFE-side electrode.

The above results show that the connection of electrodes greatly affects the TENG stimulation efficiency. When flipping the electrode connection, the TENG stimulation efficiency may decrease and even decrease to no stimulation effect. This can be explained with the illustration in Figure 4f. Current

output of the TENG forms two asymmetrical peaks in response to the pressing and releasing phase of the TENG deformation. For the PTFE side (blue), during the pressing and releasing process, it gains electron first and then loses electron. Thus, the PTFE-side electrode experiences a positive current peak followed by a negative current peak. In contrast, the aluminum-side electrode experiences a negative−positive current stimulation. To effectively depolarize the neuron membrane, positive−negative and negative−positive TENG current stimulation have different stimulation efficiency. Before flipping the electrode connection, the aluminum-side electrode which locates closer to motoneurons experiences positive−negative current stimulation and effectively induces muscle contraction. After flipping the electrode connection, the aluminum-side electrode experiences the less efficient positive−negative current stimulation and fails to activate the nearby motoneurons.

Modeling of How Motoneuron Activation Is Affected by Electrode-Motoneuron Position and Stimulation Waveform Polarity. After demonstrating that we were able to use TENG to directly power muscle stimulation, we proceeded to investigate how the stimulation efficiency was affected by electrode-motoneuron position and stimulation waveform polarity. To study the interaction between different electrode sites and muscle tissue, we developed a distributed-parameter circuit model. The entire muscle tissue, including the motoneurons and extracellular medium, was modeled as a distributed-parameter circuit network. The detailed circuit configuration of each block in this network was determined by its biological features. Here, motoneurons were represented by parallel RLC components (green blocks in Figure 5a),[72−75] and muscle fibers were represented by RC components (blue blocks in Figure 5a).[76]

In Figure 5a, fixed electrode sites (positive electrode site between P3 and P4; negative electrode site between P9 and P10) were selected to deliver negative-first biphasic square current input. Voltage waveforms upon different blocks (P1 to P12) were modeled and shown in Figure 5b. For these different blocks, voltage amplitude changed, and the polarity
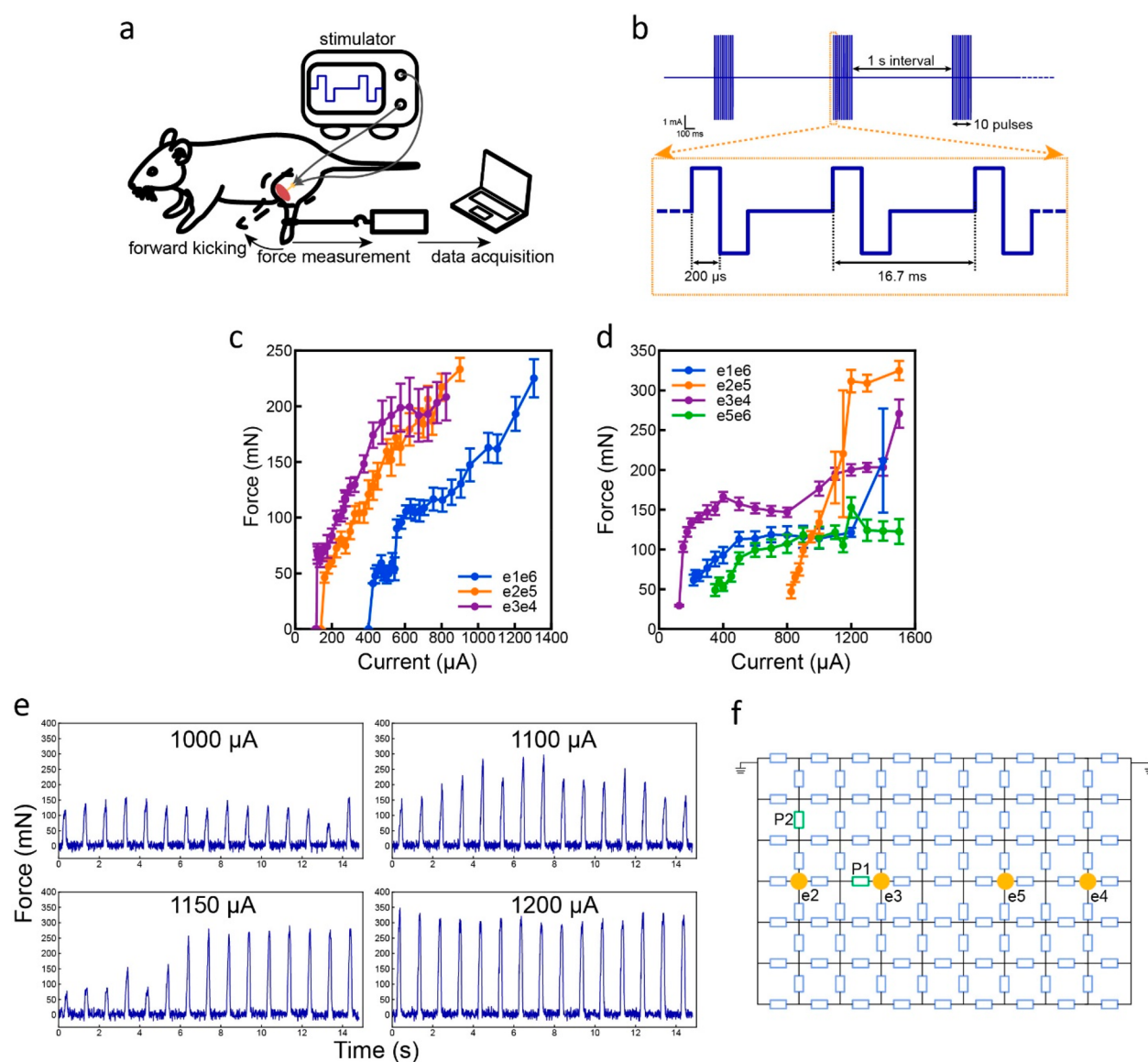
Figure 6. Study of electrode-neuron influence on stimulation efficiency. (a) Testing setup. (b) Square wave stimulation current waveform. (c) Force mapping on one animal. (d) Force mapping on another animal. (e) Force profile measured at four current amplitude for the orange force mapping curve in panel d. (f) Possible electrode-neuron position.

also switched. The blocks that were next to the electrode sites (P3 and P4; P9 and P10) had the largest voltage amplitude. Meanwhile, voltage polarity gradually changed from negative-first to positive-first when the position changed from P1 to P12. Changing trends of peak amplitude and polarity (green lines in Figure 5b) agreed with the results using conventional method of electric field distribution modeling (Figure S4). In another situation (Figure 5c), two motoneuron blocks were fixed (P1 and P2), while the spacing between electrode sites was increased (positive electrode site between P1 and P2 was fixed; negative electrode site changed from E1 to E8). The voltage waveforms on P1 and P2 (Figure 5d and Figure 5e) showed an opposite changing trend. Peak amplitude of the block outside electrode sites (P1) and between electrode sites (P2) increased and decreased with increasing electrode spacing, respectively.

In Vivo Measurement of How Motoneuron Activation Is Affected by Electrode-Motoneuron Position and Current Waveform Polarity. To test whether the stimulation efficiency dependence on electrode-motoneuron position and electrode connection was unique for TENG stimulation, we applied the conventional square wave for further investigation using the *in vivo* force measurement setup (Figure 6a). Square wave had fixed polarity and pulse width, and only the current amplitude was adjusted (Figure 6b). Because of the unknown electrode-motoneuron position after electrode implantation, stimulating efficiency using the same electrode pair would vary in different experimental trials. In Figure 6c, electrode sites with the largest spacing (e1 and e6) showed the minimum stimulation efficiency. However, in another experiment (Figure 6d), electrode sites of e1 and e6 showed the medium stimulation efficiency.

Two force mapping curves (e2e5, orange and e3e4, purple) were selected from Figure 6d. There was a sudden force increment accompanied by an abnormally large error bar for the orange curve. We speculate this error bar is a sign of an additional group of motoneurons starting to be recruited with increasing current amplitude. In our experiments, the
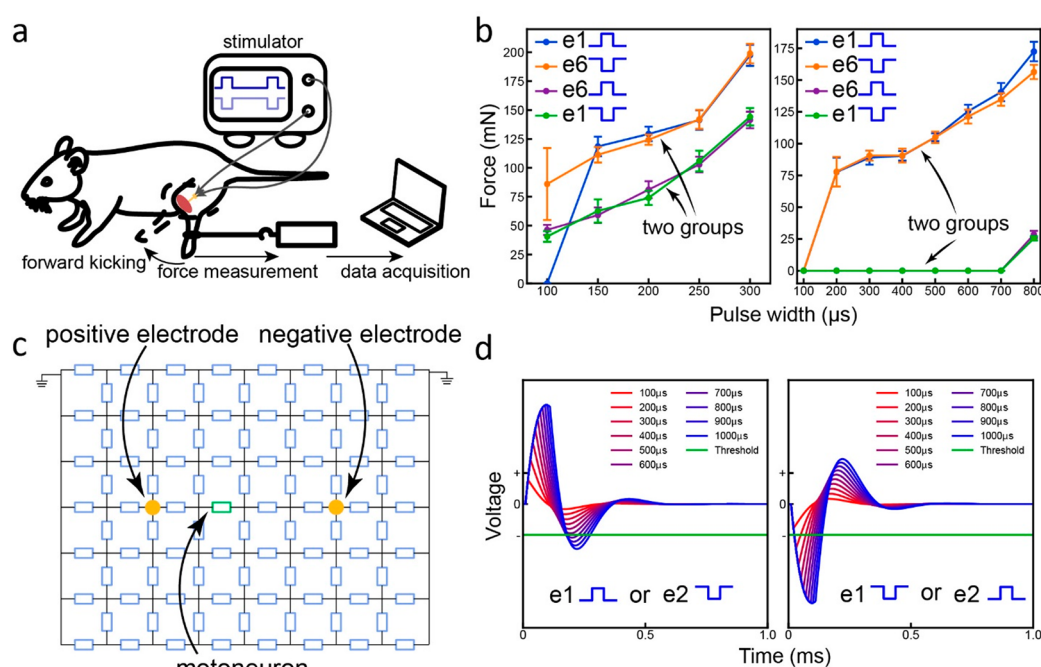
Figure 7. Study of waveform polarity influence on stimulation efficiency. (a) Testing setup. (b) Measurement in two animals. (c) Modeling circuit. (d) Voltage waveforms on the motoneuron.

measured force is the summed-up effect generated by multiple groups of activated motoneurons. When an additional group of motoneurons starts to be recruited by stimulation, although the total force will be higher than activating one group alone, the force generated by this second group of motoneurons is still low and unstable at this stage. Therefore, the measured force curve will show a large error bar at this current. Then when current amplitude further increases, the stimulation strength of this second group of motoneurons will be higher, which results in a stable force output, making the error bar return to a normal level. This abnormal high error bar should only occur within a certain current range. Figure 6e shows the force profile measured at this transition range (1000 μA to 1200 μA) of the orange curve in Figure 6d. When current amplitude was high enough (1200 μA), the force profile recovered to a stable condition. Here a simple modeling case is demonstrated. The corresponding electrode pairs of these two curves were modeled in the circuit network. The locations of the two target motoneurons (P1 and P2) were captured to fit the force mapping curves. At low stimulation current, both E1 and E2 electrode pairs could only stimulate P1. However, when current increases, E2 started to stimulate another motoneuron P2, while E1 had no influence on P2. From this modeling, the relative locations of the two motoneurons with respect to the electrode sites can be roughly estimated.

We then investigated how waveform polarity affects motoneuron activation using the force measurement setup in Figure 7a. As shown in Figure 5b, the polarity of voltage waveforms at different positions will not be the same. This polarity is not only determined by motoneuron position, but also determined by which electrode is connected to the positive terminal of current source. Figure 7b uses force mapping curves measured in the two independent *in vivo* experiments to demonstrate this principle. One force mapping curve was measured at small pulse width range (100−300 μs), and the other was measured at large pulse width range (100−

800 μs). Two electrode sites (e1 and e6) of the furthest distance on our polyimide electrode were used. Force mapping curves were the same when e1 delivered positive current or e6 delivered negative current (blue and orange curves). Force mapping curves were also the same when e1 delivered negative current or e6 delivered positive current (purple and green curves). In each measurement, the four recruitment curves formed two groups of different changing trend with increasing pulse width. The flipping of voltage waveform polarity caused the voltage waveforms to exceed threshold voltage in different patterns, so that the two groups had totally different changing trends with increasing pulse width.

Figure 7c shows a distributed-parameter circuit to model how stimulation current waveform affects motoneuron activation. Two electrode sites were connected to current source to deliver monophasic square wave current pulses of different pulse widths. Voltage waveform by applying positive pulses from the positive electrode and negative pulses from the negative electrode were the same (Figure 7d). Similarly, voltage waveform by applying negative pulses from the positive electrode and positive pulses from the negative electrode were the same (Figure 7d). Although the voltage waveforms in Figure 7d were just of opposite polarity, changing trend of the effective voltage area with increasing pulse width was completely different. This explains what we observed in Figure 7b.

CONCLUSION

We present a self-powered system of TENG and flexible multiple-channel intramuscular electrode for electrical muscle stimulation. The multiple-channel intramuscular electrode allows mapping of motoneurons that are sparsely distributed in the muscle tissue, to enable high efficiency TENG electrical muscle stimulation with short-circuit current of 35 μA, which is much lower than the typical mA-level muscle stimulation. We find the TENG muscle stimulation efficiency is strongly

affected by two factors, namely, the electrode-motoneuron position, and stimulation waveform polarity. When electrodes are closer to motoneuron distributions, stimulation efficiency is improved. Meanwhile, stimulation efficiency differs when the stimulation waveform polarity is switched. We further investigate using the conventional square wave and confirm that these two factors universally affect electrical muscle stimulation of various input current waveforms. Our work validates the possibility of direct TENG muscle stimulation. In addition, the involvement of the multiple-channel intramuscular electrode provides guidance for practical applications of using this self-powered system, as it allows stimulation efficiency optimization. With the recent development of TENGs,[77−80] we believe this self-powered system can be used for electrical muscle stimulation to treat muscle function loss.

EXPERIMENTAL SECTION

***In Vivo* Electrode Implantation.** All experiments were conducted according to protocols approved by the Institutional Animal Care and Use Committee at the National University of Singapore. Six Sprague−Dawley rats (around 450 g) were used for the acute experiments. Anesthesia was induced with isoflurane (Aerrane, Baxter Healthcare Corp., USA). Carprofen (Rimadyl, Zoetis, Inc., USA) was injected for pain relief before surgery. After the rat was anesthetized, fur on the leg was gently removed by a shaver. Then the skin was disinfected with 70% ethanol wipes, and an incision was made with a surgical blade to expose the TA muscle. The flexible multiple-channel intramuscular electrode was sutured into the TA muscle belly with the help of a suture wire.

Force Data Collection and Analysis. The anesthetized rat was fixed on a stand, and the ankle of left leg was connected to a dual-range force sensor (Vernier, USA). This force sensor was connected to a laptop through a DAQ. LabView (National Instruments, USA) was used for on-site result visualization during the measurements. After the measurements, MATLAB was used for data analysis.

Modeling. The modeling was performed on MATLAB. First, a circuit description was performed in Simulink (MathWorks, USA). Then current inputs of different waveforms were recursively fed to the circuit model, and the voltage responses of the targeted RC component were collected.

ASSOCIATED CONTENT

Ⓢ Supporting Information

The Supporting Information is available free of charge on the ACS Publications website at DOI: 10.1021/acsnano.9b00140.

> TENG muscle stimulation movie (AVI)
> TENG muscle stimulation with force measurement movie (AVI)
> Fabrication of TENG; fabrication of flexible multiple-channel intramuscular electrode; stimulation efficiency difference when flipping electrode connection; fabrication process of TENGs; fabrication process of flexible multiple-channel intramuscular electrode; flexible multiple-channel intramuscular electrode; simulation of electric field spatial distribution; working mechanism of stacked-layer TENGs; flipping electrode connection (PDF)

AUTHOR INFORMATION

Corresponding Author
*E-mail: elelc@nus.edu.sg.

ORCID Ⓞ
Chengkuo Lee: 0000-0002-8886-3649

Author Contributions
¶J.W. and H.W. contributed equally to this work.

REFERENCES

(1) Katz, B.; Miledi, R. The Effect of Prolonged Depolarization on Synaptic Transfer in the Stellate Ganglion of the Squid. *J. Physiol.* **1971**, *216*, 503−512.

(2) Boutry, C. M.; Negre, M.; Jorda, M.; Vardoulis, O.; Chortos, A.; Khatib, O.; Bao, Z. A Hierarchically Patterned, Bioinspired e-Skin Able to Detect the Direction of Applied Pressure for Robotics. *Sci. Robot.* **2018**, *3*, 6914.

(3) Tee, B. C.-K.; Chortos, A.; Berndt, A.; Nguyen, A. K.; Tom, A.; McGuire, A.; Lin, Z. C.; Tien, K.; Bae, W.-G.; Wang, H.; Mei, P.; Chou, H.; Cui, B.; Deisseroth, K.; Ng, T. N.; Bao, Z. A Skin-Inspired Organic Digital Mechanoreceptor. *Science* **2015**, *350*, 313−316.

(4) Lipomi, D. J.; Vosgueritchian, M.; Tee, B. C. K.; Hellstrom, S. L.; Lee, J. A.; Fox, C. H.; Bao, Z. Skin-like Pressure and Strain Sensors Based on Transparent Elastic Films of Carbon Nanotubes. *Nat. Nanotechnol.* **2011**, *6*, 788−792.

(5) Bariya, M.; Shahpar, Z.; Park, H.; Sun, J.; Jung, Y.; Gao, W.; Nyein, H. Y. Y.; Liaw, T. S.; Tai, L.-C.; Ngo, Q. P.; Chao, M.; Zhao, Y.; Hettick, M.; Cho, G.; Javey, A. Roll-to-Roll Gravure Printed Electrochemical Sensors for Wearable and Medical Devices. *ACS Nano* **2018**, *12*, 6978−6987.

(6) Nyein, H. Y. Y.; Tai, L.-C.; Ngo, Q. P.; Chao, M.; Zhang, G. B.; Gao, W.; Bariya, M.; Bullock, J.; Kim, H.; Fahad, H. M.; Javey, A. A Wearable Microfluidic Sensing Patch for Dynamic Sweat Secretion Analysis. *ACS Sensors* **2018**, *3*, 944−952.

(7) Bariya, M.; Nyein, H. Y. Y.; Javey, A. Wearable Sweat Sensors. *Nat. Electron.* **2018**, *1*, 160−171.

(8) Luo, N.; Dai, W.; Li, C.; Zhou, Z.; Lu, L.; Poon, C. C. Y.; Chen, S.-C.; Zhang, Y.; Zhao, N. Flexible Piezoresistive Sensor Patch Enabling Ultralow Power Cuffless Blood Pressure Measurement. *Adv. Funct. Mater.* **2016**, *26*, 1178−1187.

(9) Gong, S.; Schwalb, W.; Wang, Y.; Chen, Y.; Tang, Y.; Si, J.; Shirinzadeh, B.; Cheng, W. A Wearable and Highly Sensitive Pressure Sensor with Ultrathin Gold Nanowires. *Nat. Commun.* **2014**, *5*, 3132.

(10) Jeong, J.-W.; Kim, M. K.; Cheng, H.; Yeo, W.-H.; Huang, X.; Liu, Y.; Zhang, Y.; Huang, Y.; Rogers, J. A. Capacitive Epidermal Electronics for Electrically Safe, Long-Term Electrophysiological Measurements. *Adv. Healthcare Mater.* **2014**, *3*, 642−648.

(11) Kim, D.-H.; Lu, N.; Ma, R.; Kim, Y.-S.; Kim, R.-H.; Wang, S.; Wu, J.; Won, S. M.; Tao, H.; Islam, A.; Yu, K. J.; Kim, T.; Chowdhury, R.; Ying, M.; Xu, Li.; Li, M.; Chung, H.; Keum, H.; McCormick, M.; et al. Epidermal Electronics. *Science* **2011**, *333*, 838−843.

(12) Hammock, M. L.; Chortos, A.; Tee, B. C. K.; Tok, J. B. H.; Bao, Z. 25th Anniversary Article: The Evolution of Electronic Skin (e-Skin): A Brief History, Design Considerations, and Recent Progress. *Adv. Mater.* **2013**, *25*, 5997−6038.

(13) Wang, X.; Dong, L.; Zhang, H.; Yu, R.; Pan, C.; Wang, Z. L. Recent Progress in Electronic Skin. *Adv. Sci.* **2015**, *2*, 1500169.

(14) Zhang, X. S.; Han, M.; Kim, B.; Bao, J. F.; Brugger, J.; Zhang, H. All-in-One Self-Powered Flexible Microsystems Based on Tribo-electric Nanogenerators. *Nano Energy* **2018**, *47*, 410−426.

(15) Yoon, H. J.; Ryu, H.; Kim, S. W. Sustainable Powering Triboelectric Nanogenerators: Approaches and the Path towards Efficient Use. *Nano Energy* **2018**, *51*, 270−285.

(16) Askari, H.; Hashemi, E.; Khajepour, A.; Khamesee, M. B.; Wang, Z. L. Towards Self-Powered Sensing Using Nanogenerators for Automotive Systems. *Nano Energy* **2018**, *53*, 1003−1019.

(17) Paosangthong, W.; Torah, R.; Beeby, S. Recent Progress on Textile-Based Triboelectric Nanogenerators. *Nano Energy* **2019**, *55*, 401−423.

(18) Payne, C. J.; Wamala, I.; Abah, C.; Thalhofer, T.; Saeed, M.; Bautista-Salinas, D.; Horvath, M. A.; Vasilyev, N. V.; Roche, E. T.; Pigula, F. A.; Walsh, C. J. An Implantable Extracardiac Soft Robotic Device for the Failing Heart: Mechanical Coupling and Synchroniza-tion. *Soft Robot* **2017**, *4*, 241−250.

(19) Arab Hassani, F.; Mogan, R. P.; Gammad, G. G. L.; Wang, H.; Yen, S.-C.; Thakor, N. V.; Lee, C. Toward Self-Control Systems for Neurogenic Underactive Bladder: A Triboelectric Nanogenerator Sensor Integrated with a Bistable Micro-Actuator. *ACS Nano* **2018**, *12*, 3487−3501.

(20) Guo, Y.; Jiang, S.; Grena, B. J. B.; Kimbrough, I. F.; Thompson, E. G.; Fink, Y.; Sontheimer, H.; Yoshinobu, T.; Jia, X. Polymer Composite with Carbon Nanofibers Aligned during Thermal Drawing as a Microelectrode for Chronic Neural Interfaces. *ACS Nano* **2017**, *11*, 6574−6585.

(21) Apollo, N. V.; Maturana, M. I.; Tong, W.; Nayagam, D. A. X.; Shivdasani, M. N.; Foroughi, J.; Wallace, G. G.; Prawer, S.; Ibbotson, M. R.; Garrett, D. J. Soft, Flexible Freestanding Neural Stimulation and Recording Electrodes Fabricated from Reduced Graphene Oxide. *Adv. Funct. Mater.* **2015**, *25*, 3551−3559.

(22) Lee, S.; Peh, W. Y. X.; Wang, J.; Yang, F.; Ho, J. S.; Thakor, N. V.; Yen, S.; Lee, C. Toward Bioelectronic Medicine-Neuromodulation of Small Peripheral Nerves Using Flexible Neural Clip. *Adv. Sci.* **2017**, *4*, 1700149.

(23) Boretius, T.; Badia, J.; Pascual-Font, A.; Schuettler, M.; Navarro, X.; Yoshida, K.; Stieglitz, T. A Transverse Intrafascicular Multichannel Electrode (TIME) to Interface with the Peripheral Nerve. *Biosens. Bioelectron.* **2010**, *26*, 62−69.

(24) Badia, J.; Boretius, T.; Andreu, D.; Azevedo-Coste, C.; Stieglitz, T.; Navarro, X. Comparative Analysis of Transverse Intrafascicular Multichannel, Longitudinal Intrafascicular and Multipolar Cuff Electrodes for the Selective Stimulation of Nerve Fascicles. *J. Neural Eng.* **2011**, *8*, 036023.

(25) Xiang, Z.; Yen, S.; Sheshadri, S.; Wang, J.; Lee, S.; Liu, Y.; Liao, L.; Thakor, N. V.; Lee, C. Progress of Flexible Electronics in Neural Interfacing - A Self-Adaptive Non-Invasive Neural Ribbon Electrode for Small Nerves Recording. *Adv. Mater.* **2016**, *28*, 4472−4479.

(26) Wei, X.; Luan, L.; Zhao, Z.; Li, X.; Zhu, H.; Potnis, O.; Xie, C. Nanofabricated Ultraflexible Electrode Arrays for High-Density Intracortical Recording. *Adv. Sci. (Weinheim, Baden-Wurttemberg, Ger.* **2018**, *5*, 1700625.

(27) Luan, L.; Wei, X.; Zhao, Z.; Siegel, J. J.; Potnis, O.; Tuppen, C. A.; Lin, S.; Kazmi, S.; Fowler, R. A.; Holloway, S.; Dunn, A. K.; Chitwood, R. A.; Xie, C. Ultraflexible Nanoelectronic Probes Form Reliable, Glial Scar-Free Neural Integration. *Sci. Adv.* **2017**, *3*, e1601966.

(28) Ethier, C.; Oby, E. R.; Bauman, M. J.; Miller, L. E. Restoration of Grasp Following Paralysis through Brain-Controlled Stimulation of Muscles. *Nature* **2012**, *485*, 368−371.

(29) Bonizzato, M.; Pidpruzhnykova, G.; DiGiovanna, J.; Shkorbatova, P.; Pavlova, N.; Micera, S.; Courtine, G. Brain-Controlled Modulation of Spinal Circuits Improves Recovery from Spinal Cord Injury. *Nat. Commun.* **2018**, *9*, 3015.

(30) Asboth, L.; Friedli, L.; Beauparlant, J.; Martinez-Gonzalez, C.; Anil, S.; Rey, E.; Baud, L.; Pidpruzhnykova, G.; Anderson, M. A.; Shkorbatova, P.; Batti, L.; Pages, S.; Kreider, J.; Schneider, B. L.; Barraud, Q.; Courtine, G. Cortico−reticulo−spinal Circuit Reorgan-ization Enables Functional Recovery after Severe Spinal Cord Contusion. *Nat. Neurosci.* **2018**, *21*, 1−13.

(31) Handa, Y.; Yagi, R.; Hoshimiya, N. Application of Functional Electrical Stimulation to the Paralyzed Extremities. *Neurol. Med. Chir. (Tokyo).* **1998**, *38*, 784−788.

(32) Dupont Salter, A.-C.; Richmond, F. J. R.; Loeb, G. E. Prevention of Muscle Disuse Atrophy by Low-Frequency Electrical Stimulation in Rats. *IEEE Trans. Neural Syst. Rehabil. Eng.* **2003**, *11*, 218−226.

(33) Loeb, G. E.; Davoodi, R. The Functional Reanimation of Paralyzed Limbs. *IEEE Eng. Med. Biol. Mag.* **2005**, *24*, 45−51.

(34) Grandjean, P. A.; Mortimer, J. T. Recruitment Properties of Monopolar and Bipolar Epimysial Electrodes. *Ann. Biomed. Eng.* **1986**, *14*, 53−66.

(35) Uhlir, J. P.; Triolo, R. J.; Davis, J. A.; Bieri, C. Performance of Epimysial Stimulating Electrodes in the Lower Extremities of Individuals with Spinal Cord Injury. *IEEE Trans. Neural Syst. Rehabil. Eng.* **2004**, *12*, 279−287.

(36) Schmit, B. D.; Mortimer, J. T. The Tissue Response to Epimysial Electrodes for Diaphragm Pacing in Dogs. *IEEE Trans. Biomed. Eng.* **1997**, *44*, 921−930.

(37) Akers, J. M.; Peckham, P. H.; Keith, M. W.; Merritt, K. Tissue Response to Chronically Stimulated Implanted Epimysial and Intramuscular Electrodes. *IEEE Trans. Rehabil. Eng.* **1997**, *5*, 207−220.

(38) Memberg, W. D.; Peckham, P. H.; Keith, M. W. A Surgically-Implanted Intramuscular Electrode for an Implantable Neuromuscular Stimulation System. *IEEE Trans. Rehabil. Eng.* **1994**, *2*, 80−91.

(39) Loeb, G. E.; Peck, R. A.; Moore, W. H.; Hood, K. BION System for Distributed Neural Prosthetic Interfaces. *Med. Eng. Phys.* **2001**, *23*, 9−18.

(40) Mallela, V. S.; Ilankumaran, V.; Rao, N. S. Trends in Cardiac Pacemaker Batteries. *Indian Pacing Electrophysiol. J.* **2004**, *4*, 201−212.

(41) Lee, K. L.; Lau, C.-P.; Tse, H.-F.; Echt, D. S.; Heaven, D.; Smith, W.; Hood, M. First Human Demonstration of Cardiac Stimulation with Transcutaneous Ultrasound Energy Delivery: Implications for Wireless Pacing with Implantable Devices. *J. Am. Coll. Cardiol.* **2007**, *50*, 877−883.

(42) Seo, D.; Neely, R. M.; Shen, K.; Singhal, U.; Alon, E.; Rabaey, J. M.; Carmena, J. M.; Maharbiz, M. M. Wireless Recording in the Peripheral Nervous System with Ultrasonic Neural Dust. *Neuron* **2016**, *91*, 529−539.

(43) Ho, J. S.; Yeh, A. J.; Neofytou, E.; Kim, S.; Tanabe, Y.; Patlolla, B.; Beygui, R. E.; Poon, A. S. Y. Wireless Power Transfer to Deep-Tissue Microimplants. *Proc. Natl. Acad. Sci. U. S. A.* **2014**, *111*, 7974−7979.

(44) Hwang, G.-T.; Kim, Y.; Lee, J.-H.; Oh, S.; Jeong, C. K.; Park, D. Y.; Ryu, J.; Kwon, H.; Lee, S.-G.; Joung, B.; Kwon, H.; Lee, S.; Joung, B.; Kim, D.; Lee, K. J. Self-Powered Deep Brain Stimulation *via* a Flexible PIMNT Energy Harvester. *Energy Environ. Sci.* **2015**, *8*, 2677−2684.

(45) Hwang, G.-T.; Park, H.; Lee, J.-H.; Oh, S.; Park, K.-I.; Byun, M.; Park, H.; Ahn, G.; Jeong, C. K.; No, K.; Kwon, H.; Lee, S.; Joung, B.; Lee, K. J. Self-Powered Cardiac Pacemaker Enabled by Flexible Single Crystalline PMN-PT Piezoelectric Energy Harvester. *Adv. Mater.* **2014**, *26*, 4880−4887.

(46) Dagdeviren, C.; Yang, B. D.; Su, Y.; Tran, P. L.; Joe, P.; Anderson, E.; Xia, J.; Doraiswamy, V.; Dehdashti, B.; Feng, X.; Lu, B.; Poston, R.; Khalpey, Z.; Ghaffari, R.; Huang, Y.; Slepian, M. J.; Rogers, J. A. Conformal Piezoelectric Energy Harvesting and Storage from Motions of the Heart, Lung, and Diaphragm. *Proc. Natl. Acad. Sci. U. S. A.* **2014**, *111*, 1927−1932.

(47) Dagdeviren, C.; Joe, P.; Tuzman, O. L.; Park, K.-I.; Lee, K. J.; Shi, Y.; Huang, Y.; Rogers, J. A. Recent Progress in Flexible and Stretchable Piezoelectric Devices for Mechanical Energy Harvesting, Sensing and Actuation. *Extrem. Mech. Lett.* **2016**, *9*, 269−281.

(48) Kim, D. H.; Shin, H. J.; Lee, H.; Jeong, C. K.; Park, H.; Hwang, G. T.; Lee, H. Y.; Joe, D. J.; Han, J. H.; Lee, S. H.; Kim, J.; Joung, B.; Lee, K. J. *In Vivo* Self-Powered Wireless Transmission Using

Biocompatible Flexible Energy Harvesters. *Adv. Funct. Mater.* **2017**, 27, 1700341.

(49) Li, N.; Yi, Z.; Ma, Y.; Xie, F.; Huang, Y.; Tian, Y.; Dong, X.; Liu, Y.; Shao, X.; Li, Y.; Jin, L.; Liu, J.; Xu, Z.; Yang, B.; Zhang, H. Direct Powering a Real Cardiac Pacemaker by Natural Energy of a Heartbeat. *ACS Nano* **2019**, DOI: 10.1021/acsnano.8b08567.

(50) Hansen, B. J.; Liu, Y.; Yang, R.; Wang, Z. L. Hybrid Nanogenerator for Concurrently Harvesting Biomechanical and Biochemical Energy. *ACS Nano* **2010**, 4, 3647−3652.

(51) Olivo, J.; Carrara, S.; De Micheli, G. Energy Harvesting and Remote Powering for Implantable Biosensors. *IEEE Sens. J.* **2011**, 11, 1573−1586.

(52) Kerzenmacher, S.; Ducrée, J.; Zengerle, R.; von Stetten, F. Energy Harvesting by Implantable Abiotically Catalyzed Glucose Fuel Cells. *J. Power Sources* **2008**, 182, 1−17.

(53) Zhu, G.; Lin, Z.-H.; Jing, Q.; Bai, P.; Pan, C.; Yang, Y.; Zhou, Y.; Wang, Z. L. Toward Large-Scale Energy Harvesting by a Nanoparticle-Enhanced Triboelectric Nanogenerator. *Nano Lett.* **2013**, 13, 847−853.

(54) Chen, B. D.; Tang, W.; He, C.; Jiang, T.; Xu, L.; Zhu, L. P.; Gu, G. Q.; Chen, J.; Shao, J. J.; Luo, J. J.; Wang, Z. L. Ultrafine Capillary-Tube Triboelectric Nanogenerator as Active Sensor for Microliquid Biological and Chemical Sensing. *Adv. Mater. Technol.* **2018**, 3, 1700229.

(55) Wang, Z. L.; Jiang, T.; Xu, L. Toward the Blue Energy Dream by Triboelectric Nanogenerator Networks. *Nano Energy* **2017**, 39, 9−23.

(56) Chen, B. D.; Tang, W.; He, C.; Deng, C. R.; Yang, L. J.; Zhu, L. P.; Chen, J.; Shao, J. J.; Liu, L.; Wang, Z. L. Water Wave Energy Harvesting and Self-Powered Liquid-Surface Fluctuation Sensing Based on Bionic-Jellyfish Triboelectric Nanogenerator. *Mater. Today* **2018**, 21, 88−97.

(57) Chen, B.; Tang, W.; Jiang, T.; Zhu, L.; Chen, X.; He, C.; Xu, L.; Guo, H.; Lin, P.; Li, D.; Shao, J.; Wang, Z. L. Three-Dimensional Ultraflexible Triboelectric Nanogenerator Made by 3D Printing. *Nano Energy* **2018**, 45, 380−389.

(58) Chen, B. D.; Tang, W.; Zhang, C.; Xu, L.; Zhu, L. P.; Yang, L. J.; He, C.; Chen, J.; Liu, L.; Zhou, T.; Wang, Z. L. Au Nanocomposite Enhanced Electret Film for Triboelectric Nanogenerator. *Nano Res.* **2018**, 11, 3096−3105.

(59) Zheng, Q.; Zou, Y.; Zhang, Y.; Liu, Z.; Shi, B.; Wang, X.; Jin, Y.; Ouyang, H.; Li, Z.; Wang, Z. L. Biodegradable Triboelectric Nanogenerator as a Life-Time Designed Implantable Power Source. *Sci. Adv.* **2016**, 2, e1501478.

(60) Zheng, Q.; Zhang, H.; Shi, B.; Xue, X.; Liu, Z.; Jin, Y.; Ma, Y.; Zou, Y.; Wang, X.; An, Z.; Tang, W.; Zhang, W.; Yang, F.; Liu, Y.; Lang, X.; Xu, Z.; Li, Z.; Wang, Z. L. *In Vivo* Self-Powered Wireless Cardiac Monitoring *via* Implantable Triboelectric Nanogenerator. *ACS Nano* **2016**, 10, 6510−6518.

(61) Liu, Z.; Ma, Y.; Ouyang, H.; Shi, B.; Li, N.; Jiang, D.; Xie, F.; Qu, D.; Zou, Y.; Huang, Y.; Li, H.; Zhao, C.; Tan, P.; Yu, M.; Fan, Y.; Zhang, H.; Wang, Z. L.; Li, Z. Transcatheter Self-Powered Ultrasensitive Endocardial Pressure Sensor. *Adv. Funct. Mater.* **2019**, 29, 1807560.

(62) Zheng, Q.; Shi, B.; Fan, F.; Wang, X.; Yan, L.; Yuan, W.; Wang, S.; Liu, H.; Li, Z.; Wang, Z. L. *In Vivo* Powering of Pacemaker by Breathing-Driven Implanted Triboelectric Nanogenerator. *Adv. Mater.* **2014**, 26, 5851−5856.

(63) Jiang, W.; Li, H.; Liu, Z.; Li, Z.; Tian, J.; Shi, B.; Zou, Y.; Ouyang, H.; Zhao, C.; Zhao, L.; Sun, R.; Zheng, H.; Fan, Y.; Wang, Z. L.; Li, Z. Fully Bioabsorbable Natural-Materials-Based Triboelectric Nanogenerators. *Adv. Mater.* **2018**, 30, 1801895.

(64) Shi, B.; Li, Z.; Fan, Y. Implantable Energy-Harvesting Devices. *Adv. Mater.* **2018**, 30, 1801511.

(65) Guo, W.; Zhang, X.; Yu, X.; Wang, S.; Qiu, J.; Tang, W.; Li, L.; Liu, H.; Wang, Z. L. Self-Powered Electrical Stimulation for Enhancing Neural Differentiation of Mesenchymal Stem Cells on Graphene-Poly(3,4-Ethylenedioxythiophene) Hybrid Microfibers. *ACS Nano* **2016**, 10, 5086−5095.

(66) Fu, Y.; Zhang, M.; Dai, Y.; Zeng, H.; Sun, C.; Han, Y.; Xing, L.; Wang, S.; Xue, X.; Zhan, Y.; Zhang, Y. A Self-Powered Brain Multi-Perception Receptor for Sensory-Substitution Application. *Nano Energy* **2018**, 44, 43−52.

(67) Dai, Y.; Fu, Y.; Zeng, H.; Xing, L.; Zhang, Y.; Zhan, Y.; Xue, X. A Self-Powered Brain-Linked Vision Electronic-Skin Based on Triboelectric-Photodetecing Pixel-Addressable Matrix for Visual-Image Recognition and Behavior Intervention. *Adv. Funct. Mater.* **2018**, 28, 1800275.

(68) Zhang, X.-S.; Han, M.-D.; Wang, R.-X.; Meng, B.; Zhu, F.-Y.; Sun, X.-M.; Hu, W.; Wang, W.; Li, Z.-H.; Zhang, H.-X. High-Performance Triboelectric Nanogenerator with Enhanced Energy Density Based on Single-Step Fluorocarbon Plasma Treatment. *Nano Energy* **2014**, 4, 123−131.

(69) Lee, S.; Wang, H.; Wang, J.; Shi, Q.; Yen, S.-C.; Thakor, N. V.; Lee, C. Battery-Free Neuromodulator for Peripheral Nerve Direct Stimulation. *Nano Energy* **2018**, 50, 148−158.

(70) Lee, S.; Wang, H.; Shi, Q.; Dhakar, L.; Wang, J.; Thakor, N. V.; Yen, S.-C.; Lee, C. Development of Battery-Free Neural Interface and Modulated Control of Tibialis Anterior Muscle *via* Common Peroneal Nerve Based on Triboelectric Nanogenerators (TENGs). *Nano Energy* **2017**, 33, 1−11.

(71) Peckham, P. H.; Knutson, J. S. Functional Electrical Stimulation for Neuromuscular Applications. *Annu. Rev. Biomed. Eng.* **2005**, 7, 327−360.

(72) Vazifehkhah Ghaffari, B.; Kouhnavard, M.; Aihara, T.; Kitajima, T. Mathematical Modeling of Subthreshold Resonant Properties in Pyloric Dilator Neurons. *BioMed Res. Int.* **2015**, 2015, 135787.

(73) Thomas, A. Memristor-Based Neural Networks. *J. Phys. D: Appl. Phys.* **2013**, 46, 093001.

(74) Cheng, K.; Zou, C.-H. Biomedicine and Informatics Model of Alzheimer's Disease. *Am. J. Biochem. Biotechnol.* **2007**, 3, 145−149.

(75) Wu, F.; Ma, J.; Zhang, G. A New Neuron Model under Electromagnetic Field. *Appl. Math. Comput.* **2019**, 347, 590−599.

(76) Morris, C.; Lecar, H. Voltage Oscillations in the Barnacle Giant Muscle Fiber. *Biophys. J.* **1981**, 35, 193−213.

(77) Lee, S.; Shi, Q.; Lee, C. From Flexible Electronics Technology in the Era of IoT and Artificial Intelligence toward Future Implanted Body Sensor Networks. *APL Mater.* **2019**, 7, 031302.

(78) Shi, Q.; He, T.; Lee, C. More than Energy Harvesting − Combining Triboelectric Nanogenerator and Flexible Electronics Technology for Enabling Novel Micro-/Nano-Systems. *Nano Energy* **2019**, 57, 851−871.

(79) Chen, L.; Shi, Q.; Sun, Y.; Nguyen, T.; Lee, C.; Soh, S. Controlling Surface Charge Generated by Contact Electrification: Strategies and Applications. *Adv. Mater.* **2018**, 30, 1−15.

(80) Lee, S.; Lee, C. Toward Advanced Neural Interfaces for the Peripheral Nervous System (PNS) and Their Future Applications. *Curr. Opin. Biomed. Eng.* **2018**, 6, 130−137.